

Adsorption Mechanisms and Transport Behavior between Selenate and Selenite on Different Sorbents

Michelle MV Snyder¹ and Wooyong Um^{1,2*}

¹Energy and Environment Directorate, Pacific Northwest National Laboratory, Richland, WA 99354, USA

²Division of Advanced Nuclear Engineering, Pohang University of Science and Technology (POSTECH), Pohang, South Korea (ROK)

*Corresponding author: Wooyong Um, Energy and Environment Directorate, Pacific Northwest National Laboratory, Richland, WA 99354, USA, Tel: 509-372-6227; Fax: 509- 371-7249; E-mail: wooyong.um@pnnl.gov

Received date: March 12, 2014; Accepted date: April 22, 2014; Published date : April 30, 2014

Copyright: © 2014 Um W, et al. This is an open-access article distributed under the terms of the Creative Commons Attribution License, which permits unrestricted use, distribution, and reproduction in any medium, provided the original author and source are credited.

Abstract

Adsorption of different oxidation species of selenium (Se), selenate (SeO_4^{2-}) and selenite (SeO_3^{2-}), with varying pHs (2-10) and ionic strengths ($I=0.01$ M, 0.1 M and 1.0 M NaNO_3) was measured on quartz, aluminum oxide, and synthetic iron oxide (ferrihydrite) using batch reactors to obtain a more detailed understanding of the adsorption mechanisms (e.g., inner- and outer-sphere complex). In addition to the batch experiments with single minerals contained in native Hanford Site sediment, additional batch adsorption studies were conducted with native Hanford Site sediment and groundwater as a function of 1) total Se concentration (from 0.01 to 10 mg L^{-1}) and 2) soil to solution ratios ($1:20$ and $1:2$ grams per mL). Results from these batch studies were compared to a set of saturated column experiments that were conducted with natural Hanford sediment and groundwater spiked with either selenite or selenate to observe the transport behavior of these species. Both batch and column results indicated that selenite adsorption was consistently higher than that of selenate in all experimental conditions used. These different adsorption mechanisms between selenite and selenate result in the varying mobility of Se in the subsurface environment and explain the dependence on the oxidation species.

Keywords: Selenite; Selenate; Inner-sphere complex; Outer-sphere complex; Adsorption

Introduction

Selenium (Se) is required for adequate nutrition, but at high concentrations Se can be toxic to humans and animals. In humans, exposure to high concentrations of Se can result in loss of hair and fingernails, cause numbness in the fingers or toes, and weaken the body's nervous and circulatory systems [1]. Similar to humans, animals also have a narrow range between deficient and toxic concentrations of Se. Contamination of Se, caused by irrigation drainage, was discovered in 1983 at Kesterson Reservoir in California and was linked to deformities in waterfowl [2]. Because of the environmental and human health risks associated with Se, the U.S. Environmental Protection Agency (EPA) has determined the Maximum Contaminant Level (MCL) for Se in drinking water to be 0.05 parts per million (ppm) [1]. The MCL for Se is sometimes exceeded in areas that have a large amount of mining, industrial activity, and seleniferous soils [1,3]. Furthermore, the planned disposal of immobilized low-activity waste (ILAW) glass containing ^{79}Se ($t_{1/2}=2.9 \times 10^5$ years) [4], located in the 200 East area of the Hanford Site, southeastern Washington State, may also pose a significant risk for radioactive Se release [5]. Dissolution of the vitrified radioactive waste matrix containing ^{79}Se , a fission product of ^{235}U , could result in Se release into the environment. Depending on the rate of glass dissolution, Se that is released from the host matrix can be transported through the vadose zone and can contaminate the underlying sediment and groundwater aquifer. To prevent spreading of radioactive Se contamination, a more in depth understanding of the migration of Se in the environment is required [5-7].

The ability to predict the fate and transport of toxic and radioactive Se in subsurface environments requires an understanding of the sorption processes that occur at the mineral-water interface. The effect of sorption on contaminant mobility is determined by molecular level processes involving the sorption complex, which can be divided into three distinct mechanisms: 1) adsorption (inner-sphere vs. outer-sphere complex), 2) absorption, and 3) surface precipitation [8,9]. Although each individual process is extremely important, adsorption is expected to play the largest role in the mobility of most contaminants, including Se.

The process of adsorption occurs when adsorbate accumulates on the surface of a solid (adsorbent) at the solid-water interface, where the ions, liquid, or gas molecules are held onto the surface without the development of a three-dimensional molecular arrangement [9]. Adsorption not only influences the distribution of contaminants between the aqueous phase and particulate matter, but it also affects the electrostatic properties of particles and the reactivity of mineral surfaces [10].

Oxyanions selenite (SeO_3^{2-}) and selenate (SeO_4^{2-}) are dominant in both mild and strong oxidizing conditions and are the most mobile aqueous species of Se [11]. Numerous studies have been conducted to evaluate the adsorption behavior of these oxidation species, SeO_3^{2-} and SeO_4^{2-} [12-15]. Many of these studies focused on the effects of various environmental factors on SeO_3^{2-} and SeO_4^{2-} adsorption. For example, Balistrieri and Chao studied the effects of pH, temperature, total Se concentrations, and competing anions on the adsorption of SeO_3^{2-} on goethite (FeOOH) [12]. Results demonstrated that SeO_3^{2-} adsorption increased with decreasing pH and an increase in the solid to solution ratio. However, adsorption of SeO_3^{2-} decreased with an increase in the total Se concentration and in the presence of competing anions such as phosphate, silicate or citrate which bind strongly to the

goethite surface. Zhang and Sparks conducted studies to determine the mechanisms of SeO_3^{2-} and SeO_4^{2-} at the goethite/water interface [16]. Their results suggested that SeO_3^{2-} forms a stronger inner-sphere surface complex whereas SeO_4^{2-} forms a weaker bonded outer-sphere surface complex. Gonzalez et al. [17] studied an iron/manganese oxide nanomaterial as a potential material for the treatment technology and removal of SeO_3^{2-} and SeO_4^{2-} . Results found sorption on the nanomaterial to be pH independent (between pH 2 to 6) and sorption of both oxyanions to be effected by the presence of phosphate with a larger decrease in SeO_4^{2-} sorption than SeO_3^{2-} . The addition of sulfate only effected the sorption of SeO_4^{2-} and the addition of nitrate and chloride had no effect on the sorption of either SeO_3^{2-} or SeO_4^{2-} . Additional studies conducted to determine sorption onto simple mineral systems include Zonkhoeva [18] that studied the sorption of SeO_3^{2-} on natural zeolites and Yoon, et al. [19] which studied sorption of SeO_4^{2-} onto zero-valent iron. In general, studies that compared adsorption of SeO_3^{2-} and SeO_4^{2-} consistently found that SeO_3^{2-} is more rapidly adsorbed than SeO_4^{2-} and lower pH conditions favor stronger Se adsorption [20].

Although the information discussed above represents a majority of the research on the adsorption of SeO_3^{2-} and SeO_4^{2-} , few studies are available on the transport of these oxyanions under real environmental conditions. Therefore, the purpose of this study was to evaluate how changes in the Se redox state (SeO_3^{2-} or SeO_4^{2-}) will affect adsorption and transport of Se in native Hanford Site soil and groundwater conditions. Hanford Site groundwater contains several of the anions expected to compete with Se for available adsorption sites. To evaluate the adsorption and transport behavior of SeO_3^{2-} or SeO_4^{2-} , a set of batch adsorption and saturated column experiments were conducted with Hanford sediment and groundwater spiked with either SeO_3^{2-} or SeO_4^{2-} . In addition to these experiments, a set of batch adsorption experiments using pure single minerals [e.g., quartz (SiO_2), aluminum oxide (Al_2O_3), and iron oxide (2-line ferrihydrite, ($\text{Fe}(\text{OH})_3$)] contained in native Hanford sediments were also conducted as a function of ionic strength and pH. The two principal objectives of these experiments were 1) to determine the mineral phase that has the largest effect on Se adsorption and 2) to use macroscopic methods to determine whether or not SeO_3^{2-} and SeO_4^{2-} form an inner- or outer-sphere complex on the mineral surface. These and other results obtained from this study will improve our understanding of the release and transport of Se from the radioactive waste glass that will be buried in the Integrated Disposal Facility (IDF) on the Hanford Site.

Materials and Methods

Hanford sediment characterization

Hanford sediment was utilized as an adsorbent to determine the adsorption of SeO_3^{2-} and SeO_4^{2-} . The sediment was collected from borehole C3177 (299-E24-21) located in the center of the 200 East Area, northeast corner of the ILAW disposal site, at the Hanford Site Nuclear Reservation located in southeastern Washington state [21]. The sediment, C3177-110, was obtained from borehole C3177 by homogenizing four two-foot long (71.0 cm) cores to provide sufficient volume of representative Hanford sediment.

The Hanford formation¹ can be subdivided into three main layers within the ILAW disposal facility and consists of pebble to boulder-sized gravel and fine to coarse grained sand with interbedded, thin silt and/or clay beds [22]. Composite C3177-110 is representative of Hanford formation layer II and is dominated by sand. Particle size distribution was determined by wet sieve and hydrometer methods, and revealed that the sediment is comprised of gravel (3.85 wt%), sand (88.6 wt%), silt (6.19 wt%), and clay (1.36 wt%) [21]. X-ray diffraction (XRD) analysis revealed that the Hanford sediment is dominated by quartz and feldspars with lesser amounts of chlorite, mica and amphibole, which is typical of Hanford Site sediments (Table 1). Additional sediment characterization included moisture content, carbon content, BET surface area, bulk sediment composition determined by x-ray fluorescence (XRF), and mineralogical content of clay determined by X-ray diffraction (XRD). These results are summarized in Tables 1 and 2.

Mineral phase on bulk sample (wt%) ¹						Moisture content (wt%)	Surface area (m ² /g)		Carbon content (wt %) ²	
Q	A	P	K	M	C	bulk	clay	total	inorganic	
45	1	25	19	9	2	2.76	5.11	41.8	0.20	0.19

Table 1: Characterization of the composite sediment including moisture content, carbon content and mineralogy of bulk sample by XRD (modified from [21]). 1) Mineral phase indicates Q (quartz), A (Amphibole), P (Plagioclase), K (K-feldspar), M (Mica), and C (Chlorite). 2) Organic carbon content is determined by difference between total and inorganic carbon contents.

Mineral phase of clay (wt %)				Bulk composition of major element oxides (wt %)									
Smectite	Illite	Chlorite	Kaolinite	SiO ₂	Al ₂ O ₃	TiO ₂	Fe ₂ O ₃	MnO	CaO	MgO	K ₂ O	Na ₂ O	P ₂ O ₅
26	51	16	7	70.4	13.2	0.672	4.91	0.077	3.72	1.87	2.54	2.87	0.153

Table 2: Characterization of the composite sample including clay mineralogy by XRD and major elemental composition by XRF (modified from [21]).

Preparation and characterization of pure single minerals

White quartz sand (SiO_2), 50-70 mesh size (Aldrich Chemical Company) was acid treated (to remove any impurities) with analytical grade concentrated sulfuric acid (H_2SO_4) for two days, rinsed several

times with double deionized (DDI) water, and oven dried at 85°C for 48 hours prior to use. The cleaning of quartz was based on a procedure used by [23].

¹ The term "Hanford formation" is used informally to describe Pleistocene cataclysmic flood deposits within the Pasco Basin. It is not a formalized stratigraphic unit.

Synthetic aluminum oxide (Al_2O_3), or transition Alumina (C-33), is a porous and high-surface area synthetic aluminum oxide with a specific surface area of $110 \text{ m}^2\text{g}^{-1}$ [24]. The alumina (C-33) used in this study was created by the partial dehydration of aluminum hydroxides and oxyhydroxides, where the final product is a completely dehydrated oxide (corundum) [25]. Additional characterization of this aluminum oxide can be found in reference [25].

The synthetic iron oxide [ferrihydrite, $\text{Fe}(\text{OH})_3$] preparation was based on Schwertmann and Cornell [26]. The ferrihydrite was prepared by neutralizing 0.2 M ferric nitrate [$\text{Fe}(\text{NO}_3)_3 \cdot 9\text{H}_2\text{O}$], from Aldrich Chemical Company; (analytical grade) with 1.0 M sodium hydroxide (NaOH), from J.T. Baker; (analytical grade). The resulting solid was washed by successive centrifuging and decanting with double deionized water (DDI). The solid was filtered from solution by vacuum using a $0.45 \mu\text{m}$ filter unit. Powder X-ray diffraction (XRD) patterns were obtained using a Scintag, Pad-V X-Ray Diffractometer (XRD) with a Cu source. The ferrihydrite was analyzed on the XRD using a 2-Theta range from 2° to 65° , a step size of 0.01° , and a 2 second count time at each step. The XRD pattern was identified as ferrihydrite (Figure 1) using the JADE software (MDI, Livermore, California).

Elements (cations)	Concentration (mg/L)	Elements (anions)	Concentration (mg/L)
Ca	59.5	HCO_3	169
Si	28	SO_4	70.6
S	26.1	Cl	18.9
Na	24.4	NO_3	9.44
Mg	22	F	0.45
K	7.5		
Sr	0.236		
Zn	0.283		
Cr	0.002		
Mo	0.002		
pH (measured)=8.04; electrical conductivity=0.474 mS/cm			

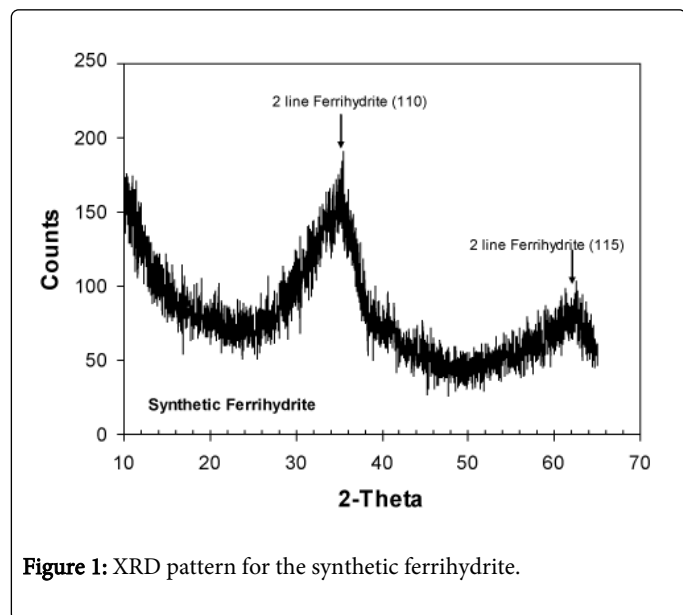


Figure 1: XRD pattern for the synthetic ferrihydrite.

Batch adsorption experiments

Groundwater used for the adsorption and column experiments with Hanford sediment was collected from the well 699-49-100C located in the 600 area of the Hanford Site. Well 699-49-100C is an uncontaminated background monitoring well. Analyses of cations and anions in this groundwater were conducted using an inductively coupled plasma-optical emission spectroscopy (ICP-OES) and an Ion Chromatograph (IC), respectively. The pH was measured with a solid-state pH electrode and a pH meter calibrated with buffers 7 and 10. The electrical conductivity (EC) was measured using a Pharmacia Biotech Conductivity Monitor. Approximately 2 to 3 milliliters of filtered sample were measured in the conductivity meter and compared to potassium chloride standards with a range of 0.001 to 1.0 M. Chemical compositions as well as the pH and EC values for this groundwater are shown in Table 3.

Table 3: Chemical composition, pH, and conductivity of groundwater (699-49-100C).

Batch adsorption experiments were conducted in duplicate for adsorption of SeO_3^{2-} and SeO_4^{2-} on the C3177 sediment. Particles greater than 2 mm were removed prior to using the sediment and the sediment was pre-equilibrated with the Hanford groundwater. The groundwater was added to the sediments, the sediments were shaken overnight, centrifuged, and the pH measured and then the supernatant was decanted. This was repeated three times until the pH of the supernatant groundwater did not change after contact overnight with the sediment. Pre-equilibration was done to ensure that reactions that occurred during laboratory batch sorption experiments were not due to any other reactions (e.g. dissolution) except adsorption. Batch experiments were conducted in 15 mL polypropylene centrifuge tubes with solid to solution ratio of 1:20 or 1:2 (gram per mL). Initial concentrations (C_0) of SeO_3^{2-} and SeO_4^{2-} ranged from 0.01 to 10 mg L^{-1} and were prepared by the addition of Na_2SeO_3 or Na_2SeO_4 , respectively, to the groundwater.

Additional batch adsorption experiments were conducted for SeO_3^{2-} and SeO_4^{2-} on single minerals such as quartz, aluminum and iron oxide under varying ionic strength ($I=0.01$ to 1.0 M NaNO_3) and pH (2 to 10) conditions. Experiments were conducted at a solid to solution ratio of 1:100 (gram per mL) with the addition of 1 mg L^{-1} of Na_2SeO_3 or Na_2SeO_4 , respectively, in NaNO_3 solution. The pH was adjusted by the addition of 0.01 M nitric acid (HNO_3) or 0.01 M sodium hydroxide (NaOH).

Hanford sediment or pure single minerals were contacted with solution spiked with SeO_3^{2-} or SeO_4^{2-} . After shaking for 7 days on a slowly moving platform shaker, the slurry sediment sample was centrifuged to separate the solids out of solution. The final pH was measured, and the supernatant was decanted and filtered through a $0.45 \mu\text{m}$ syringe filter. Solution was analyzed for Se concentration using an inductively coupled plasma mass spectrometer (ICP-MS). The difference in C_0 and the final concentration of SeO_3^{2-} or SeO_4^{2-} in solution was used for adsorption of Se onto the sediments.

In addition, two different types of experimental control samples were also prepared to determine 1) whether or not SeO_3^{2-} and SeO_4^{2-}

adsorbed onto the walls of the test vessels and 2) to determine the contribution of natural SeO_3^{2-} and SeO_4^{2-} released from the unreacted Hanford sediment. The final solution was also analyzed for Se concentrations, and showed negligible Se adsorption onto the test tube walls and no natural Se release from the sediment.

Calculation of partition coefficient (Kd)

The partition coefficient (K_d) is a measure of adsorption and is defined as the ratio of the amount of an adsorbate sorbed on a solid to the amount of adsorbate still in solution at equilibrium [27]. The expression is as follows:

$$K_d = \frac{A_i}{C_i}$$

where A_i =adsorbate on the solid at equilibrium ($\mu\text{g g}^{-1}$); C_i =adsorbate remaining in solution at equilibrium ($\mu\text{g mL}^{-1}$). For the batch studies conducted during this experiment, the K_d values were calculated using the following equation:

$$K_d = \frac{V_w(C_o - C_i)}{M_{sed}C_i}$$

where V_w =known volume of solution (ml); C_o =initial concentration of adsorbate ($\mu\text{g mL}^{-1}$); M_{sed} =known mass of sediment (μg).

Column experiments and determination of retardation factor (R_f)

Two borosilicate glass columns (Kontes Chromaflex Chromatography columns, $L=10$ cm, diameter= 2.5 cm) were uniformly packed with sediment C3177-110 after removing gravel (>2 mm size fraction). Two individual columns were utilized to evaluate the mobility of SeO_3^{2-} and SeO_4^{2-} , respectively. An AVI Micro 210A Infusion Pump was used to control the constant flow rate. The columns were initially saturated with groundwater at a pumping rate (10 mL hour^{-1}) faster than what was used during the experiment to remove any dispersible particles and to make sure that a steady flow was maintained. Prior to conducting the Se transport experiment, the flow rate was decreased to 0.5 mL hour^{-1} until a steady flow rate was maintained. This flow rate was chosen to allow the SeO_3^{2-} and SeO_4^{2-} to remain in contact with sediment in the column for approximately one day. Prior to introducing Se, a bromide (Br) was added to the groundwater and introduced as a nonreactive tracer (no adsorption to the sediment) in each column to provide a comparison of Br mobility to the SeO_3^{2-} and SeO_4^{2-} transport results as well as hydrodynamic dispersion of the flow. Once completion of Br breakthrough in the column was attained, approximately 7 mg L^{-1} of SeO_3^{2-} or SeO_4^{2-} , respectively, spiked in groundwater was introduced to each column. The Se was pumped through the columns for approximately 13 pore volumes and the amount of Se in the effluent was measured using an inductively coupled plasma optical emission spectrometer (ICP-OES). Transport parameters were determined by curve fitting (based on the advection-dispersion equation) to the measured breakthrough curves (BTCs) using the CXTFIT code [28,29]. Breakthrough curves (BTCs) were graphically represented by plotting the relative concentration, C/C_o , for SeO_3^{2-} or SeO_4^{2-} versus pore volumes eluted. Both equilibrium and non-equilibrium (two site/two region) models were applied to analyze the experimental column breakthrough data [29]. The equilibrium model described in dimensionless terms is

$$R \frac{\partial C}{\partial T} = \frac{1}{P} \frac{\partial^2 C}{\partial Z^2} - \frac{\partial C}{\partial Z} \quad (3a) \text{ where}$$

$$T = \frac{vt}{L}, \quad Z = \frac{x}{L}, \quad C = \frac{c}{c_o}, \quad P = \frac{vL}{D}, \quad R = 1 + \frac{\rho_b K_d}{\theta} \quad (3b)$$

and T =dimensionless time equal to pore volume; t =time (T); L =column length (L); v =linear pore water velocity (LT^{-1}); Z =dimensionless distance; x =distance from the input (L); C =relative concentration between initial (c_o) and effluent (c) concentrations (ML^{-3}); P =Peclet number [-]; D =hydrodynamic dispersion coefficient (L^2T^{-1}); R [-]=retardation factor determined by the equation containing bulk density (ρ_b) (ML^{-3}), porosity (θ) (L^3L^{-3}), and distribution coefficient (K_d) (M^{-1}L^3). The non-equilibrium model is described by the following equations with dimensionless terms:

$$\beta R \frac{\partial C_1}{\partial T} + (1 - \beta) R \frac{\partial C_2}{\partial T} = \frac{1}{P} \frac{\partial^2 C_1}{\partial Z^2} - \frac{\partial C_1}{\partial Z} \quad (4a)$$

$$(1 - \beta) R \frac{\partial C_2}{\partial T} = \omega(C_1 - C_2) \quad (4b)$$

$$T = \frac{vt}{L}, \quad Z = \frac{x}{L}, \quad C_1 = \frac{c_m}{c_o}, \quad C_2 = \frac{c_{im}}{c_o} \quad (4c)$$

$$P = \frac{v_m L}{D_m} = \frac{vL}{D}, \quad v_m = \frac{q}{\theta_m}, \quad \omega = \frac{\alpha L}{v_m \theta_m}, \quad \beta = \frac{\theta_m + f \rho_b K_d}{\theta + \rho_b K_d} \quad (4d)$$

where β =dimensionless mobile fraction with mobile water fraction (f); C_1 =solute concentration in mobile water (ML^{-3}); C_2 =solute concentration in immobile water (ML^{-3}); ω =dimensionless mass transfer coefficient between mobile and immobile water regions; α =mass transfer coefficient [T^{-1}]; q =volumetric flow velocity [LT^{-1}]. The column parameters are summarized below in Table 4.

Columns	Porosity [-]	Porewater velocity (cm/day)	Pore volume (cm^3)	Bulk density (g/ cm^3)	D^1 (cm^2/day)	Retardation factor (R_f)	K_d (mL/g)
Selenite	0.29	8.17	15.3	1.59	7.09	3.10	0.38
Selenate	0.29	8.17	15.7	1.68	5.56	1.20	0.034

Table 4: Transport parameters of selenite and selenate columns. 1Hydrodynamic dispersion coefficient.

Results and Discussion

Batch selenium adsorption

Adsorption of Se on quartz under varying pHs (2-11) and ionic strengths ($I=0.01$ M to 1.0 M NaNO_3) resulted in negligible adsorption of SeO_4^{2-} regardless of pH and ionic strength conditions (Figure 2).

Even at low pH (<4) and ionic strength ($I=0.01$ M NaNO_3) conditions, no adsorption of SeO_4^{2-} was found on the quartz surfaces. Selenite (SeO_3^{2-}) showed a minor amount of adsorption ($<10\%$) onto the quartz at pH values less than 5 and only at low ionic strengths ($I=0.01$ M and 0.1 M NaNO_3). Because the adsorption was so small ($<10\%$) it is difficult to see a trend in the data. The only thing we can conclude from the data trend is that SeO_3^{2-} showed a slight high adsorption at certain pH, especially at low pH even at high ionic strength condition. An increase in SeO_3^{2-} adsorption at low pH is due to the low point of zero charge (PZC) of quartz (pHPZC ~ 2.82) [30].

At low pH conditions the surface adsorption sites for quartz are positively charged through protonation of surface charge, which is consistent with the fact that oxide and hydroxide surfaces are positively charged at lower pH and negatively charged at higher pH than that of the PZC value of the adsorbent [31]. Based on the increased SeO_3^{2-} adsorption to quartz at low ionic strengths ($I=0.01$ and 0.1 M) and low pH conditions, (although minor), SeO_3^{2-} is considered to have slightly higher adsorption affinity to quartz than SeO_4^{2-} which exhibits no detectable adsorption onto quartz at all conditions studied.

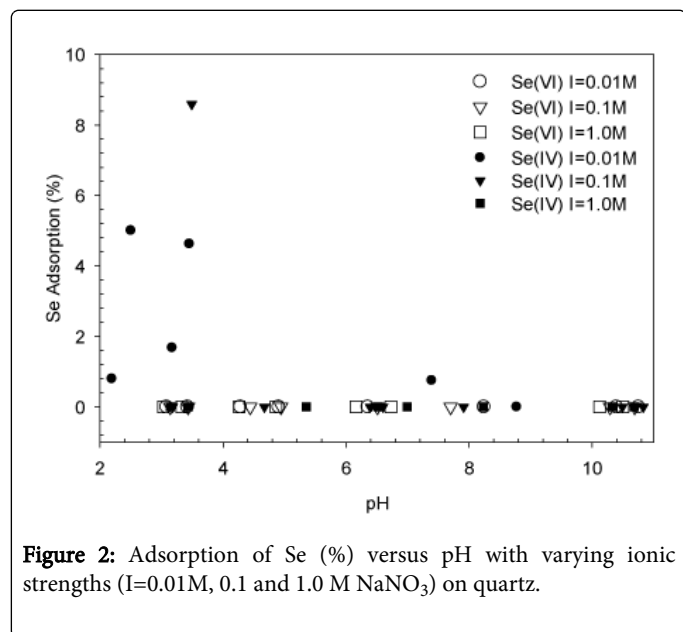


Figure 2: Adsorption of Se (%) versus pH with varying ionic strengths ($I=0.01\text{M}$, 0.1 and 1.0 M NaNO_3) on quartz.

Adsorption of SeO_3^{2-} on synthetic ferrihydrite at varying pH (4-8) and at fixed ionic strength ($I=0.1$ M NaNO_3) resulted in nearly 100% adsorption (98.4% to 99.9%) (Figure 3). However, SeO_4^{2-} displayed adsorption ranging from 6 to 82%, with decreasing adsorption as pH increased, with higher percentages of uptake at the lower pH ranges (<7). The high adsorption of SeO_4^{2-} at $\text{pH}<7$ was attributed to the higher PZC of iron oxide ($\text{pH}_{\text{PZC}}=8.5$ to 8.8) compared to that of quartz ($\text{pH}_{\text{PZC}} \sim 2.82$) [31]. There were more discernable adsorption differences between SeO_3^{2-} and SeO_4^{2-} as the pH changed, indicating that SeO_3^{2-} has a higher adsorption affinity to Fe oxide similar to the Se adsorption results on quartz. In addition, the elevated adsorption of SeO_3^{2-} compared to SeO_4^{2-} onto the Fe oxide at all pH conditions also suggests a higher adsorption affinity of SeO_3^{2-} which agrees with the results of Se adsorption on the quartz.

Adsorption results for Se onto aluminum oxide under different ionic strengths ($I=0.01$ to 1.0 M NaNO_3) and varying pHs (4 - 10) are shown in Figure 4. Selenite adsorption on aluminum oxide was greater than 96% at $\text{pH}<8.5$ with no discernable effect from varying ionic strength ($I=0.01$ and 1.0 M NaNO_3). High adsorption affinity of SeO_3^{2-} on alumina oxide at low pHs was attributed to the high surface area ($110 \text{ m}^2 \text{ g}^{-1}$) and PZC of alumina oxide ($\text{pH}_{\text{PZC}}=8.5$) [25], resulting in positive surface charges due to protonation of alumina oxide surface at lower pH ($\text{pH}<8.5$). Decreasing adsorption of SeO_3^{2-} was found as pH increased, especially at higher pHs (>8.0) because of the negatively charged alumina surfaces at high pHs. In contrast, SeO_4^{2-} adsorption onto aluminum oxide was largely affected by changes in ionic strength from 0.01 M to 1.0 M NaNO_3 . Selenate

adsorption decreased as both ionic strength and pH increased (Figure 3).

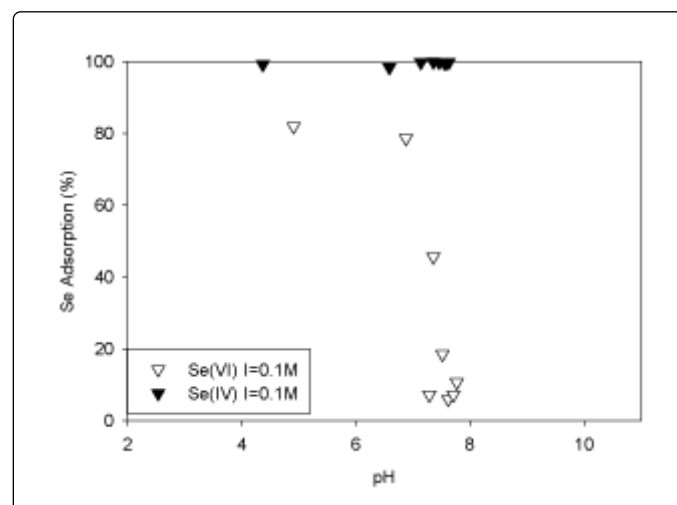


Figure 3: Adsorption of Se (%) versus pH with ionic strengths $I=0.1\text{M}$ NaNO_3 on ferrihydrite.

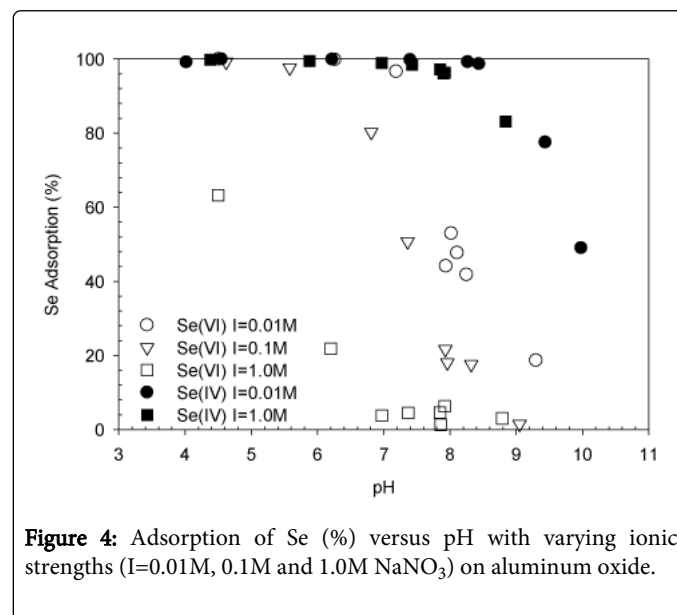


Figure 4: Adsorption of Se (%) versus pH with varying ionic strengths ($I=0.01\text{M}$, 0.1M and 1.0M NaNO_3) on aluminum oxide.

As ionic strength increased from $I=0.01$ M to 1.0 M NaNO_3 , there is an increase in concentration of anions (e.g., NO_3^-) from the background electrolyte, which competes with SeO_4^{2-} for available adsorption sites. The ionic-strength dependence of SeO_4^{2-} adsorption suggests an outer-sphere surface complex, while the SeO_3^{2-} adsorption suggests formation of an inner-sphere surface complex because of the independent adsorption behavior of SeO_3^{2-} with respect to varying background ionic strengths. Due to a weaker electrostatic bond, outer-sphere complexes are less stable and considered to be relatively weakly binding. A strong dependence on ionic strength is typically found in species that form outer-sphere surface complexes [31]. Conversely, the ionic strength independence of SeO_3^{2-} adsorption suggests a stronger covalent bond indicative of an inner-sphere complex and direct binding of SeO_3^{2-} to the solid surface without the presence of co-adsorbed water molecules [31]. Based on the general comparison of

SeO_3^{2-} and SeO_4^{2-} adsorption on three different single minerals, SeO_3^{2-} showed a much higher adsorption affinity on all the adsorbents, suggesting a higher adsorption affinity due to a stronger bonded inner-sphere surface complex.

The adsorption of Se on the Hanford sediment was also measured using Hanford natural groundwater (Table 3). The results of Se adsorption (K_d values) were between 0 and 3 mL g^{-1} for SeO_4^{2-} , and slightly higher values for SeO_3^{2-} ranging from 0 to 22 mL g^{-1} , respectively (Figures 5 and 6). A decrease in the adsorption K_d s for both SeO_3^{2-} and SeO_4^{2-} as the initial Se concentration increased signifies the potential for nonlinear adsorption behavior for Se onto Hanford sediments. At fixed solid to solution ratio and initial Se concentration conditions, SeO_3^{2-} K_d s were higher than those found for SeO_4^{2-} , which agrees with the previous Se adsorption experiments conducted on pure single minerals.

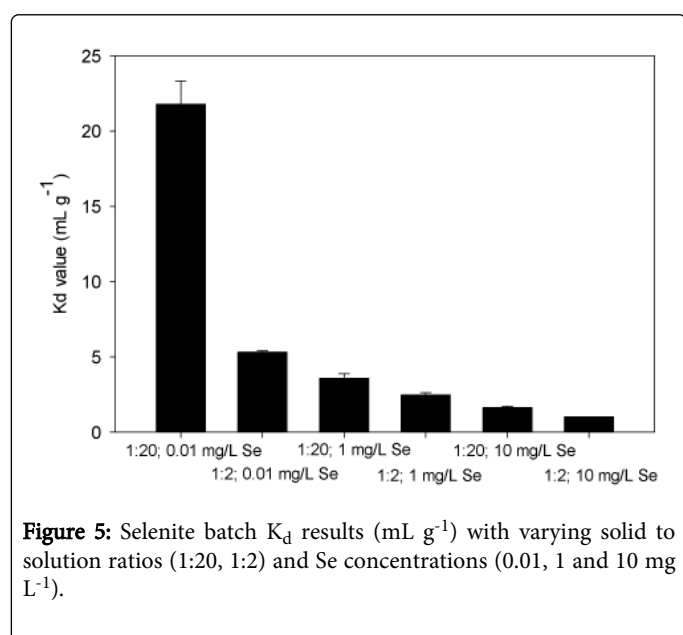


Figure 5: Selenite batch K_d results (mL g^{-1}) with varying solid to solution ratios (1:20, 1:2) and Se concentrations (0.01, 1 and 10 mg L^{-1}).

Selenium transport in column experiments

The BTCs for the nonreactive Br tracer and SeO_4^{2-} in groundwater through Hanford sediment is shown in Figure 7. The Br transport was not retarded by the Hanford sediment, resulting in a retardation value (R_f) of 1.0. The hydrodynamic dispersion coefficient for the packed columns was obtained from the CXTFIT curve fit on the Br BTC and fixed in the equilibrium model that was applied to the SeO_4^{2-} BTC. The transport of SeO_4^{2-} was slightly retarded when compared to the Br BTC and reached a relative concentration (C/C_0) of 1.0 after only 2.0 pore volumes, resulting in a R_f value of 1.2 (Table 4). The comparable retardation of Br ($R_f=1.0$) and SeO_4^{2-} ($R_f=1.2$) indicates weak adsorption affinity of SeO_4^{2-} on the Hanford sediment and was consistent with the previous batch adsorption results. Minor tailing was noticed for the SeO_4^{2-} transport at pore volume >15 (Figure 7) and showed an asymmetric BTC for SeO_4^{2-} , which suggests the presence of immobile regions resulting in physical non-equilibrium. However, the non-equilibrium model did not improve the fit results when compared to the equilibrium model, indicating that the non-equilibrium conditions were not significant for SeO_4^{2-} transport in the column.

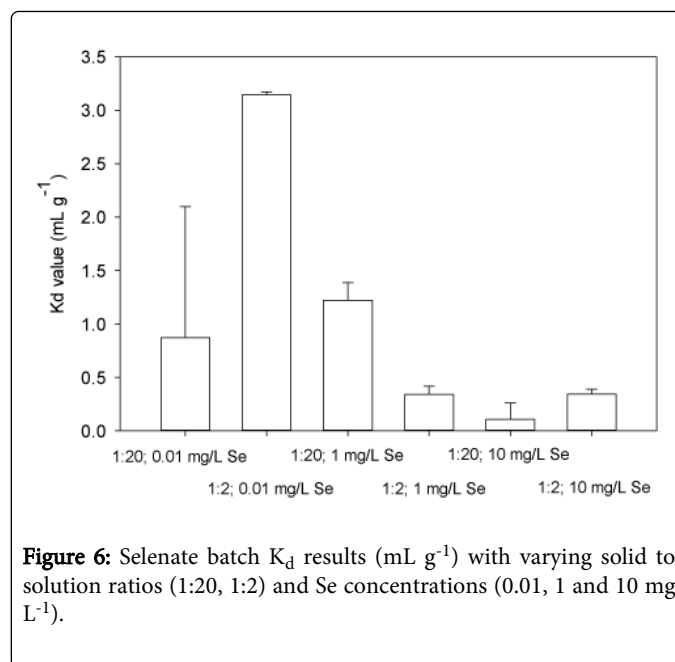


Figure 6: Selenate batch K_d results (mL g^{-1}) with varying solid to solution ratios (1:20, 1:2) and Se concentrations (0.01, 1 and 10 mg L^{-1}).

The BTCs for Br and SeO_3^{2-} with the equilibrium model fit are shown in Figure 8 and Table 4. Because the BTCs for Br and SeO_3^{2-} are fairly symmetric, an equilibrium model was used for both the Br and SeO_3^{2-} BTCs. The BTC for SeO_3^{2-} showed more retardation (with respect to Br transport) and did not reach complete breakthrough until approximately 6.5 pore volumes (Figure 8). The CXTFIT model fit to the SeO_3^{2-} column experiment resulted in an R_f value of 3.1. The SeO_3^{2-} column experiment displayed a higher adsorption resulting in more retarded transport of SeO_3^{2-} compared to the low adsorption of SeO_4^{2-} which displayed negligible retardation.

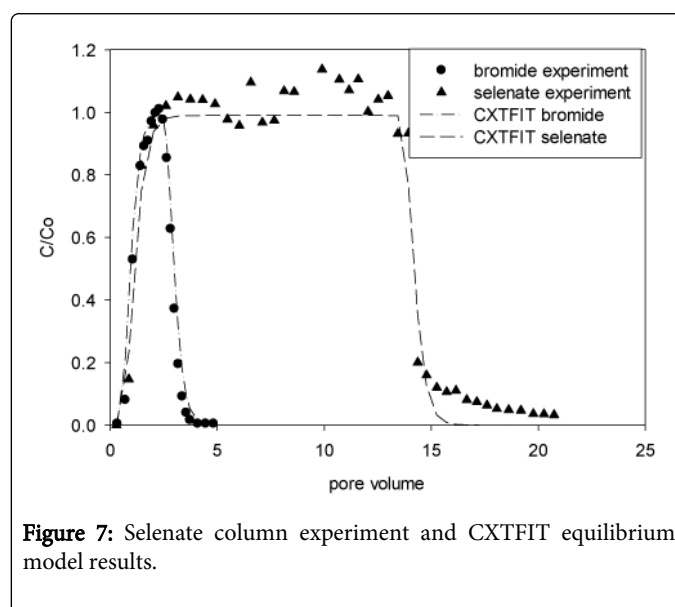


Figure 7: Selenate column experiment and CXTFIT equilibrium model results.

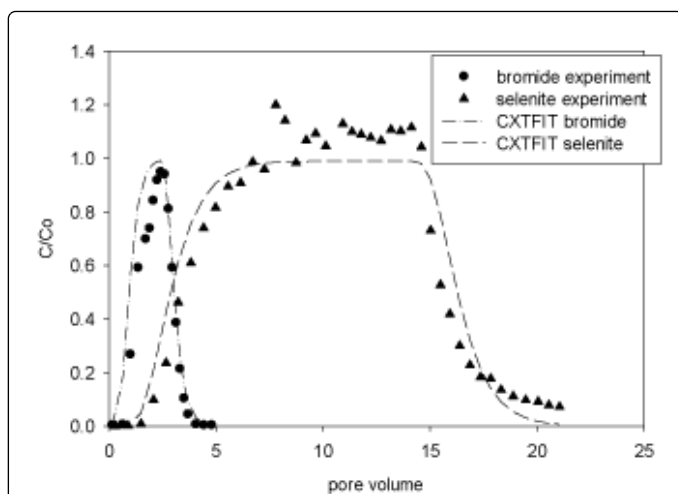


Figure 8: Selenite column experiment and CXTFIT equilibrium model results.

The calculated K_{ds} based on the retardation values obtained from the column experiments (Table 4) showed the same trend for adsorption affinity between SeO_3^{2-} and SeO_4^{2-} as observed in the batch adsorption experiments. The smaller calculated K_d values for selenite and selenate from the column experiments compared to those obtained from the batch experiments are considered to be a result of the different solid to solution ratios and contact times between the two sets of experiments. The batch and column experiments showed the same trends for SeO_3^{2-} and SeO_4^{2-} adsorption, indicating different adsorption affinities due to different adsorption mechanisms forming inter- vs. outer-sphere complexes for SeO_3^{2-} and SeO_4^{2-} , respectively. These different adsorption mechanisms should be considered in fate and transport predictions and future performance assessment activities should utilize the different mobility attributes for the Se species, SeO_3^{2-} and SeO_4^{2-} , at the Hanford Site.

Conclusions

The batch adsorption experiments on quartz, aluminum oxide and iron oxide (ferrihydrite) resulted in a higher adsorption affinity for SeO_3^{2-} than SeO_4^{2-} with higher adsorption at the lower pHs. Particularly important are the batch adsorption results on the Fe and Al oxides, which showed a higher adsorption capacity for Se, especially at circum neutral pH conditions. The SeO_3^{2-} batch adsorption results showed an ionic strength independence, while the SeO_4^{2-} adsorption showed ionic strength dependence (i.e., adsorption increased as the ionic strength decreased). Ionic strength dependence or independence in adsorption results indicates that SeO_4^{2-} displays an outer-sphere adsorption surface complex and SeO_3^{2-} forms a stronger bonded inner-sphere adsorption surface complex. The batch adsorption experiments on the Hanford sediment with natural Hanford groundwater at pH between 7.0 to 8.5 resulted in a maximum K_d value of 21.8 and 3.14 mg L^{-1} for SeO_3^{2-} and SeO_4^{2-} , respectively. In agreement with the batch adsorption experiments, the column experiments yielded negligible adsorption of SeO_4^{2-} with an R_f of 1.2, while SeO_3^{2-} showed higher adsorption with a R_f of 3.1. All experimental results at the same background conditions showed higher adsorption for SeO_3^{2-} than SeO_4^{2-} concluding that SeO_4^{2-} , the

oxidized form of Se, will be more mobile than SeO_3^{2-} in the environment.

The pure single mineral experiments resulted in minor amounts of Se adsorption on the quartz and much higher percentages of adsorption on aluminum and iron oxides. Hanford soils are dominated by quartz with lesser amounts of aluminum- and iron-bearing minerals. The composition of Hanford sediments leads to the conclusion that there will likely not be a high percentage of Se adsorption on Hanford sediment, particularly at high pH conditions similar to natural Hanford soil (7.5-8.5).

Acknowledgments

This study was conducted in support of the ILAW project with funding from the Office of River Protection (DOE) managed by CH2M-HILL Hanford Company. Eric Clayton and Steven Baum (PNNL) are also acknowledged for providing analytical support. The authors would like to thank Jeff Serne, Chris Brown and Dawn Wellman (PNNL) for their comments and suggestions to improve this manuscript. PNNL is operated by Battelle for the U.S. Department of Energy under contracts DE-AC006-76RLO 1830. A portion of this research was carried out at the POSTECH supported by WCU (World Class University) and BK21+ programs at the Division of Advanced Nuclear Engineering (DANE) in POSTECH through the National Research Foundation of Korea funded by the Ministry of Education, Science and Technology (R31-30005).

References

1. EPA (2012) National Primary Drinking Water Regulations-Inorganic Chemicals. US Environmental Protection Agency.
2. Engberg RA, Westcot DW, Delamore M, Holz DD (1998) Federal and State Perspectives on Regulation and Remediation of Irrigation-Induced Selenium Problems.
3. Mayland HF (1994) Selenium in Plant and Animal Nutrition. In: Frankenberger JWT, Sally Benson (edn) Selenium in the Environment Marcel Dekker Inc New York.
4. Lockheed Martin (2002) Chart of the Nuclides (16edn).
5. Mann FM, Puigh RJ, Rittmann PD, Kline NW, Voogd JA, et al. (1998) Hanford Immobilized Low-Activity Tank Waste Performance Assessment. US Department of Energy Richland WA.
6. Kaplan DI, Serne RJ (2000) Geochemical Data Package for the Hanford Immobilized Low-Activity Tank Waste Performance Assessment (ILAW PA). Pacific Northwest National Laboratory.
7. McGrail B, Bacon D, Serne R, Pierce E (2003) A Strategy to Assess Performance of Selected Low-Activity Waste Forms in an Integrated Disposal Facility. Pacific Northwest National Laboratory.
8. Sposito G (1982) On the Surface Complexation Model of the Oxide-Aqueous Solution Interface. *J Colloid Interface Sci* 91: 329-340.
9. Sposito G (1986) Distinguishing Adsorption from Surface Precipitation. *Geochem Process Miner Surf* 323: 217-228.
10. Stumm W (1992) Chemistry of the Solid-Water Interface: Processes at the Mineral-Water and Particle-Water Interface in Natural Systems. John Wiley and Sons Inc. Canada.
11. Breyneart E, Scheinost AC, Dom D, Rossberg A, Vancluysen J, et al. (2010) Reduction of Se(IV) in boom clay: XAS solid phase speciation. *Environ Sci Technol* 44: 6649-6655.
12. Balistriieri LS, Chao TT (1987) Selenium Adsorption by Goethite. *Soil Sci Soc Am J* 51: 1145-1151.
13. Boyle-Wight EJ, Katz LE, Hayes KF (2002a) Macroscopic Studies of the Effects of Selenate and Selenite on Cobalt Sorption to Al_2O_3 . *Environ Sci Technol* 36: 1212-1218.

14. Boyle-Wight EJ, Katz LE, Hayes KF (2002b) Spectroscopic Studies of the Effects of Selenate and Selenite on Cobalt Sorption to Al₂O₃. *Environ Sci Technol* 36: 1219-1225.
15. Duc M, Lefèvre G, Fédoroff M (2006) Sorption of selenite ions on hematite. *J Colloid Interface Sci* 298: 556-563.
16. Zhang P, Sparks DL (1990) Kinetics of Selenate and Selenite Adsorption/Desorption at the Goethite/Water Interface. *Environ Sci Technol* 24: 1848-1856.
17. Gonzalez CM, Hernandez J, Parsons JG, Gardea-Torresdey JL (2010) A Study of the Removal of Selenite and Selenate from Aqueous Solutions Using a Magnetic Iron/Manganese Oxide Nanomaterial and ICP-MS. *Microchemical Journal* 96: 324-329.
18. Zonkhoeva EL, Sanzhanova SS (2011) Infrared Spectroscopy Study of the Sorption of Selenium(IV) on Natural Zeolites. *Russian Journal of Physical Chemistry* 85: 1233-1236.
19. Yoon IH, Kim KW, Bang S, Kim MG (2011) Reduction and Adsorption Mechanisms of Selenate by Zero-valent Iron and Related Iron Corrosion. *Applied Catalysis B: Environmental* 104: 185-192.
20. Sharmasarkar S, Vance GF (2002) Selenite-Selenate Sorption in Surface Coal Mine Environment *Adv Environ Res* 7: 87-95.
21. Horton DG, Schaef HT, Serne RJ, Brown CF, Valenta MM (2003) Geochemistry of Samples From Borehole C3177 (299-E24-21). Pacific Northwest National Laboratory.
22. Reidel SP (2002) Geologic Data Package for 2005 Integrated Disposal Facility Waste Performance Assessment. Pacific Northwest National Environment.
23. Bickmore BR, Nagy KL, Young JS, Drexler JW (2001) Nitrate-cancrinite precipitation on quartz sand in simulated Hanford tank solutions. *Environ Sci Technol* 35: 4481-4486.
24. Papelis C, Roberts PV, Leckie JO (1995) Modeling the rate of cadmium and selenite adsorption on micro- and mesoporous transition aluminas. *Environ Sci Technol* 29: 1099-1108.
25. Papelis C (1992) Cadmium and Selenite Adsorption on Porous Aluminum Oxides: Equilibrium Rate of Uptake and Spectroscopic Studies Department of Civil Engineering and the Committee on Graduate Studies Stanford University, Stanford.
26. Schwertmann U, Cornell RM (2000) *Iron Oxides in the Laboratory: Preparation and Characterization*. Weinheim: Wiley-VCH.
27. EPA (1999) Understanding Variation in Partition Coefficient, K_d, Values Volume I: The K_d Model Methods of Measurement and Application of Chemical Codes. Office of Radiation and Indoor Air and Office of Environmental Restoration.
28. Parker JC, Vangenuchten MT (1984) Determining transport parameters from laboratory and field tracer experiments. *Virginia Agricultural Experiment Station Bulletin* 1-96.
29. Toride N, Leij FJ, Genuchten MT (1999) The CXTFIT Code for Estimating Transport Parameters from Laboratory or Field Tracer Experiments. US Salinity Laboratory. US Department of Agriculture Riverside California.
30. Goyne KW, Zimmerman AR, Newalkar BL, Kormarneni S, Brantley SL, et al., (2002) Surface Charge of Variable Porosity Al₂O₃(s) and SiO₂(s) Adsorbents. *Journal of Porous Materials* 9: 243-256.
31. Langmuir D (1997) *Aqueous Environmental Geochemistry*. Prentice-Hall Inc. Upper Saddle River New Jersey.